Numerical Heat Transfer, Part A, 36:449–472, 1999

1040–7782/99 $12.00 + .00

SEMI-IMPLICIT FEM ANALYSIS OF NATURAL CONVECTION IN FREEZING WATER

J. Banaszek and Y. Jaluria
Department of Mechanical and Aerospace Engineering, Rutgers University, New Brunswick, New Jersey 08903, USA

T. A. Kowalewski and M. Rebow
IPPT PAN, Polish Academy of Sciences, 00-049 Warsaw, Poland, and Warsaw University of Technology, Institute of Heat Engineering, Nowowiejska 25, 00-665 Warsaw, Poland

A semi-implicit finite element method (FEM) is presented for the two-dimensional computer simulation of solid-liquid phase change controlled by natural convection and conduction. The algorithm is based on a combination of (1) a projection method to uncouple velocity calculations from pressure calculations for incompressible fluid flow, (2) the backward Euler and explicit Adams-Bashforth schemes to effectively integrate diffusion and advection in time, and (3) an enthalpy-porosity approach to account for the latent heat effect on a fixed finite element grid. Credibility of the obtained numerical predictions is investigated through computational model verification and validation procedures. Commonly used benchmark problems are employed to verify the algorithm accuracy and performance. The natural convection of freezing pure water is studied experimentally through the use of sophisticated full-field acquisition experimental techniques. The measured velocity and temperature fields are compared with the pertinent calculations. The range of congruity of the experimental and numerical results is thoroughly studied, and potential reasons of some disparity in a local structure of the natural convection flow and in the interface shape are discussed.

INTRODUCTION

The cost-effectiveness of finite element method (FEM) calculations continues to be significant in the computer simulation of coupled fluid flow and heat transfer problems. It is commonly known that the finite difference method is superior in terms of computer storage and CPU time requirements when compared with FEM analysis. This results from a less sparse form of FEM matrices, due to the use of irregular grids and high-order polynomial interpolations of the unknown field

Received 24 September 1998; accepted 27 April 1999.
The authors acknowledge the support in part by the U.S.-Polish Commission of the Fullbright Foundation and by the Polish State Committee for Scientific Research, Grant No. 3 T09C 002 12.
Address correspondence to Jerzy Banaszek, Institute of Heat Engineering, Warsaw University of Technology, 25 Nowowiejska Str., 00-665 Warsaw, Poland. E-mail: banaszek@itc.pw.edu.pl

NOMENCLATURE

c_l	specific heat of liquid
c_s	specific heat of solid
C	porosity constant
$\mathbf{C}$	heat capacity matrix
$\mathbf{D}$	divergence matrix
f	volumetric liquid fraction
$\mathbf{F}_i$	right-hand side of momentum equation
$\mathbf{F}_\mathbf{T}$	right-hand side of energy equation
g_i	component of gravity vector
$\mathbf{G}$	gradient matrix
h	convective heat transfer coefficient
H	specific total enthalpy
$\mathbf{H}$	vector of nodal values of enthalpy
K	conductivity of mixture
$\mathbf{K}^{\mathbf{c}}$	advection matrix
$\mathbf{K}_{\mathbf{h}}^{\mathbf{c}}$	convection matrix
$\mathbf{K}^{\mathbf{d}}$	diffusion matrix
$\mathbf{K}_{\mathbf{T}}^{\mathbf{d}}$	conduction matrix
L	latent heat
M_p	shape function for geometry
$\mathbf{M}$	mass matrix
N_k	shape function for velocity and temperature
NP	number of pressure nodes in element
NP_g	number of geometric nodes in element
NV	number of velocity nodes in element
p	motion pressure
$\mathbf{p}$	vector of nodal values of pressure
P_l	shape function for pressure
Pr	Prandtl number
R	residuum of partial differential equation
Ra	Rayleigh number
Re	Reynolds number
S_{v_i}	additional source term
t	time
T	temperature
$\mathbf{T}$	vector of nodal values of temperature
v_i	velocity vector component
v_{ib}	given velocity on boundary
$\mathbf{v}_i$	vector of nodal values of velocity component
W	weighting function
x_i	global coordinate
Γ	domain boundary
Δt	time step
ζ_i	local coordinate
ϑ	kinematic viscosity
μ	dynamic viscosity
ρ	density
Φ	Lagrange multiplier of projection method
Ψ	stream function
Ω	volume of analyzed domain

Subscripts

b	boundary value
c	cold wall
env	pertinent to environment
h	hot wall
i, j	coordinate direction
k, l, p	local node number in element
l	pertinent to liquid
ref	reference state
s	pertinent to solid
Γ	pertinent to boundary Γ
Ω	pertinent to domain Ω

Superscripts

m	current iteration
n	current time step

property. But it also comes from the application of simultaneous solution algorithms, where a whole set of continuity, Navier-Stokes, and energy equations is solved concurrently, as commonly used in the early FEM analysis of incompressible fluid flows (e.g., [1, 2]). Therefore, over the last decade, attempts have been made to improve the computational efficiency of FEM simulation of field theory prob-

lems through the use of various sophisticated acceleration techniques. Most of these techniques take their origin from the finite difference methods, specifically, the following.

- Approximate solution to the Navier-Stokes equations for an incompressible fluid can be found by the use of the projection method [3, 4], where velocity is uncoupled from pressure. The keyword here is "sequential," which means first velocity is solved and then pressure, rather than simultaneously solving the coupled set of equations.
- A semi-implicit time marching scheme can be applied where viscous/diffusion terms are treated implicity, whereas advection terms are treated explicitly [4–6]. The main attribute of this approach is that it allows replacement of a set of the coupled fluid flow and heat transfer equations by several smaller symmetric linear systems where effective algebraic solvers can be used (e.g., [7]).
- In numerical modeling of solid-liquid phase change transition, the energy conservation can be analyzed via an enthalpy approach on a fixed grid [8–11]. With a correctly defined enthalpy-temperature relation, the full effect of the latent heat can be accurately modeled without the need to know an exact position of the phase interface. And thus a cumbersome front tracking algorithm is avoided.

In this paper the FEM model, based on the combination of all aforementioned techniques, is presented for coupled fluid flow and heat transfer with solid-liquid phase change phenomena occurring in a one-component or a binary system.

It is well established that an efficient computer simulation can, in many engineering problems, be a reasonable alternative to the laborious and often prohibitively expensive laboratory testing of a new product. But first the credibility of these numerical predictions must be proved. This consists of two processes: code verification and validation. Much effort has been generally focused on accuracy of numerical models. This verification procedure is based on grid refinement studies and comparison with other available solutions of some benchmark problems. Although such a study is obviously necessary, this by itself is not sufficient to establish confidence in the numerically obtained predictions. Indeed, for engineers and scientists, nature is the final jury. This means that the degree to which inevitable simplifications of physical and mathematical models reflect reality should be established. This code validation procedure is carried out by extensively comparing numerical results with trustworthy detailed experimental measurements. Both these issues are addressed in this paper in the context of the presented FEM model and its algorithm. Commonly used benchmark problems are solved to verify the algorithm accuracy and performance. Next, natural convection in pure and freezing water is studied experimentally, through the use of sophisticated full-field acquisition experimental techniques. The measured velocity and temperature fields are compared with the pertinent calculations in the code validation analysis. The paper concludes with a discussion of the scope of congruity and potential reasons for some disparity between the calculated results and experimental findings.

MATHEMATICAL MODEL AND NUMERICAL ALGORITHM

Under the assumptions that the fluid is incompressible and Newtonian and the flow is laminar, the transport of mass, momentum, and energy is governed by the following set of partial differential equations (PDEs):

$$\frac{\partial v_i}{\partial x_i} = 0$$

$$\rho \frac{\partial v_i}{\partial t} + \rho v_j \frac{\partial v_i}{\partial x_j} = \frac{\partial}{\partial x_j}\left(\mu \frac{\partial v_i}{\partial x_j}\right) + g_i(\rho - \rho_{\text{ref}}) - \frac{\partial p}{\partial x_i} + S_{v_i} \tag{1}$$

$$\frac{\partial(\rho H)}{\partial t} + v_j \frac{\partial(\rho H)}{\partial x_j} = \frac{\partial}{\partial x_j}\left(K \frac{\partial T}{\partial x_j}\right)$$

The buoyancy forces $g_i(\rho - \rho_{\text{ref}})$ are defined relative to some reference state ρ_{ref}. This means that p is the so-called motion pressure [12]. To account for the latent heat effect in the phase change, occurring over a finite range of temperatures or at a fixed temperature, the general enthalpy method of Swaminathan and Voller [11] is adopted.

The total enthalpy

$$\rho H = (1 - f)\rho_s H_s + f\rho_l H_l \tag{2}$$

is given by the weighted sum of sensible enthalpies of the solid and liquid phases and the latent heat effect L, where

$$H_s = \int_{T_{\text{ref}}}^{T} c_s(T)\, dT$$

$$H_l = \int_{T_{\text{ref}}}^{T} c_l(T)\, dT + L \tag{3}$$

The theory of mixtures is used to define the thermophysical properties in a two-phase region through a volumetric liquid fraction f, where $0 \leqslant f \leqslant 1$. This gives

$$\rho = (1 - f)\rho_s + f\rho_l$$

$$K = (1 - f)K_s + fK_l \tag{4}$$

This region, called a mushy zone, is treated as a porous medium [10, 11]. In this enthalpy-porosity model an additional source term S_{v_i} appears in the momentum

equation, where

$$S_{v_i} = -C\frac{(1-f)^2}{f^3}v_i \tag{5}$$

This mimics the Carman-Kozeny model of flow and thus, gradually, reduces velocity in the solidifying zone [10].

To obtain a discrete form of Eqs. (1), two consecutive discretization steps are carried out. First, the FEM spatial discretization, defined by the piecewise interpolations of the domain geometry and field unknowns, is used:

$$\begin{aligned} x_i(\bar{\zeta}) &= M_p(\bar{\zeta})\, x_{ip} \qquad p = 1, 2, \ldots, \mathrm{NP}_g \\ v_i(\bar{x}, t) &= N_k(\bar{x})\, v_{ik}(t) \\ T(\bar{x}, t) &= N_k(\bar{x}) T_k(t) \qquad k = 1, 2, \ldots, \mathrm{NV} \\ p(\bar{x}, t) &= P_l(\bar{x})\, p_l(t) \qquad l = 1, 2, \ldots, \mathrm{NP} \end{aligned} \tag{6}$$

along with the weighted residual approach [13]. The global error minimization technique is used where the residual R_Ω and R_Γ of the PDE and pertinent boundary conditions are weighted within a whole domain Ω and its boundary Γ through weighting functions W_k, defined in a local element basis:

$$\int_\Omega W_k R_\Omega \, d\Omega - \int_\Gamma W_k R_\Gamma \, d\Gamma = 0 \tag{7}$$

This leads to a set of ordinary differential equations in the semidiscrete FEM model, which in a commonly used matrix notation has the form

$$\begin{gathered} \mathbf{D} \cdot \mathbf{v} = \mathbf{0} \\ \mathbf{M} \cdot \frac{d\mathbf{v}_i}{dt} + [\mathbf{K}^{\mathbf{c}}(v) + \mathbf{K}^{\mathbf{d}}] \cdot \mathbf{v}_i = -\mathbf{G} \cdot \mathbf{p} + \mathbf{F}_i \qquad i = 1, 2, 3 \\ \mathbf{C} \cdot \frac{d\mathbf{H}}{dt} + \mathbf{K}_{\mathbf{h}}^{\mathbf{c}}(v) \cdot \mathbf{H} + \mathbf{K}_{\mathbf{T}}^{\mathbf{d}} \cdot \mathbf{T} = \mathbf{F}_{\mathbf{T}} \end{gathered} \tag{8}$$

Polynomials N_k and P_l are of the same order in the equal-order interpolation and are of different orders in the nonequal one [13]. In the Galerkin method, applied in the presented model, the weighting functions W_k coincide with the pertinent interpolation polynomials. $\mathbf{M}$, $\mathbf{C}$, $\mathbf{K}^{\mathbf{c}}$, $\mathbf{K}_{\mathbf{h}}^{\mathbf{c}}$, $\mathbf{K}^{\mathbf{d}}$, $\mathbf{K}_{\mathbf{T}}^{\mathbf{d}}$, $\mathbf{G}$, and $\mathbf{D}$ are the mass, heat capacity, advection, convection, diffusion, conduction, pressure gradient, and divergence matrices, respectively. Here, $\mathbf{v}_i$, $\mathbf{p}$, $\mathbf{H}$, $\mathbf{T}$, and $\mathbf{F}_i, \mathbf{F}_T$ stand for vectors of nodal unknowns and the right-hand sides of the momentum and energy equations, respectively.

The second discretization step is integration of Eq. (8) in time by use of time marching finite difference schemes to obtain a set of algebraic equations for a fully

discrete FEM model:

$$\mathbf{D}\cdot\mathbf{v}^{n+1}=\mathbf{0}$$

$$\mathbf{M}\cdot\frac{\mathbf{v}_i^{n+1}-\mathbf{v}_i^{n}}{\Delta t}+\mathbf{K}^{d}\cdot\mathbf{v}_1^{n+1}$$

$$=\mathbf{F}_i-\mathbf{G}\cdot\mathbf{p}^{n+1}-\left(\frac{3}{2}\mathbf{K}^{c}(\mathbf{v}^{n})\cdot\mathbf{v}^{n}-\frac{1}{2}\mathbf{K}^{c}(\mathbf{v}^{n-1})\cdot\mathbf{v}^{n-1}\right) \tag{9}$$

$$\mathbf{C}\cdot\frac{\mathbf{H}^{n+1}-\mathbf{H}^{n}}{\Delta t}+\mathbf{K}_{\mathbf{T}}^{\mathbf{d}}\cdot\mathbf{T}^{n+1}$$

$$=\mathbf{F}_{\mathbf{T}}-\left(\frac{3}{2}\mathbf{K}_{\mathbf{h}}^{\mathbf{c}}(\mathbf{v}^{n})\cdot\mathbf{H}^{n}-\frac{1}{2}\mathbf{K}_{\mathbf{h}}^{\mathbf{c}}(\mathbf{v}^{n-1})\cdot\mathbf{H}^{n-1}\right)$$

Pressure, which is an inherently implicit variable in an incompressible fluid model, must be treated implicitly. So the continuity equation has to be treated as such. We would be happy to extend this treatment to all other terms of the momentum and energy equations. Unfortunately, this approach creates the need for simultaneous solution of the whole set of fully coupled equations. In practice, this is prohibitively expensive and time consuming. Therefore we have used the semi-implicit approach where the diffusion terms are treated by the fully implicit Euler scheme, whereas the convective terms are calculated at two previous time steps in the explicit Adams-Bashforth method.

Further reduction of CPU time can be obtained by setting up an algorithm, where velocity calculations are uncoupled from pressure ones. In the presented code the projection methods [4] are adopted where at each time step calculations are performed in the following three-step cycle.

For a given initial kinematic pressure and divergence-free velocity fields,

1. Solve the momentum equation

$$\frac{\partial\tilde{v}_i^{n+1}}{\partial t}+v_j^{n}\frac{\partial\tilde{v}_i^{n+1}}{\partial x_j}=\frac{\partial}{\partial x_j}\left(\vartheta\frac{\partial\tilde{v}_i^{n+1}}{\partial x_j}\right)-a_p\left(\frac{1}{\rho}\frac{\partial p^{n}}{\partial x_i}\right)+\frac{1}{\rho}S_{v_i} \tag{10}$$

   with $\tilde{v}_i=v_{ib}$ on Γ, where $a_p=0$ in the Projection 1 method and $a_p=1$ when Projection 2 is used [4] to obtain the intermediate velocity field (not the solenoidal one).
2. Project this velocity vector onto the subspace of a divergence-free vector field. This leads to the Poisson equation for the projection Lagrange multiplier Φ [4]:

$$\frac{\partial}{\partial x_i}\left(\frac{\partial\Phi}{\partial x_i}\right)=\frac{\partial\tilde{v}_i}{\partial x_i}\qquad\frac{\partial\Phi}{\partial n}=0\text{ on }\Gamma$$

and to the correction of the intermediate velocity in accordance with

$$v_i^{n+1} = \tilde{v}_i^{n+1} - \frac{\partial \Phi}{\partial x_i} \tag{11}$$

3. Finally, the kinematic pressure is updated:

$$(p^{n+1}/\rho) = \frac{\Phi}{\Delta t} \qquad (p^{n+1}/\rho) = (p^n/\rho) + \frac{2}{\Delta t}\Phi \tag{12}$$

in Projection 1 or Projection 2, respectively.

Thus the projection cycle is completed.
The FEM counterpart of this algorithm has the following matrix form:

$$\mathbf{M} \cdot \frac{\tilde{\mathbf{v}}_i^{n+1} - \mathbf{v}_i^n}{\Delta t} + \mathbf{K}^{\mathbf{d}} \cdot \tilde{\mathbf{v}}_i^{n+1}$$

$$= \mathbf{F}_i - a_p \mathbf{G} \cdot \mathbf{p}^n - \left(\frac{3}{2}\mathbf{K}^{\mathbf{c}}(\mathbf{v}^n) \cdot \mathbf{v}^n - \frac{1}{2}\mathbf{K}^{\mathbf{c}}(\mathbf{v}^{n-1}) \cdot \mathbf{v}^{n-1} \right) \qquad \text{(step 1)}$$

$$\left.\begin{aligned} \mathbf{G}^{\mathbf{T}}\mathbf{M}^{-\mathbf{1}}\mathbf{G} \cdot \Phi &= -\mathbf{G}^{\mathbf{T}} \cdot \tilde{\mathbf{v}}_i^{n+1} \\ \mathbf{v}^{n+1} &= \tilde{\mathbf{v}}_i^{n+1} - \mathbf{M}^{-\mathbf{1}}\mathbf{G} \cdot \Phi \end{aligned}\right\} \qquad \text{(step 2)} \tag{13}$$

$$\mathbf{p}^{n+1}/\rho = \frac{\Phi}{\Delta t} \quad \text{or} \quad \mathbf{p}^{n+1}/\rho = \mathbf{p}^n/\rho + \frac{2}{\Delta t}\Phi \qquad \text{(step 3)}$$

The energy equation is nonlinear due to temperature dependence of both the total enthalpy and thermophysical properties in the mushy zone. Therefore, following Swaminathan and Voller [11], an iterative process is constructed at each time step, where

1. Using the previous approximation of temperature, matrices $\mathbf{K}_{\mathbf{T}}^{\mathbf{d}}(\mathbf{T}^m)$ and $\mathbf{C}(\mathbf{T}^m)$ are calculated.
2. The unknown current iteration of the total enthalpy is replaced by its Taylor series expansion:

$$H_k^{m+1} = H_k^m + \left(\frac{dH_k}{dT}\right)_m (T_k^{m+1} - T_k^m) \qquad T_k^m = H^{-1}(H_k^m) \tag{14}$$

to give the linearized energy equation

$$\left[\mathbf{K}_{\mathbf{T}}^{\mathbf{d}}(\mathbf{T}^m) + \frac{1}{\Delta t}\mathbf{C}(\mathbf{T}^m)\cdot\left(\frac{d\mathbf{H}}{d\mathbf{T}}\right)_m\right]\cdot\mathbf{T}^{m+1}$$
$$= \frac{1}{\Delta t}\mathbf{C}(\mathbf{T}^m)\cdot\left[\mathbf{H}^n - \mathbf{H}^m + \left(\frac{d\mathbf{H}}{d\mathbf{T}}\right)_m\cdot\mathbf{T}^m\right]$$
$$+\mathbf{F}_{\mathbf{T}} - \left(\frac{3}{2}\mathbf{K}_{\mathbf{h}}^{\mathbf{c}}(\mathbf{v}^n)\cdot\mathbf{H}^n - \frac{1}{2}\mathbf{K}_{\mathbf{h}}^{\mathbf{c}}(\mathbf{v}^{n-1})\cdot\mathbf{H}^{n-1}\right) \qquad (15)$$

It solution gives a new evaluation of temperature, which is next used to update enthalpy through Eq. (14).

3. The process is repeated until a relative difference between two consecutive iterations of the total enthalpy are less than a given tolerance; i.e., $\max\{\text{abs}[(H_i^{m+1} - H_i^m)/H_i^m]\} < 10^{-4}$.

MODEL VERIFICATION

To check the fluid mechanics part of the algorithm, the problem of recirculating flow in a closed square cavity, caused by the upper lid movement at constant velocity U, is calculated using the Projection 1 algorithm. This commonly used benchmark is analyzed on two different finite element grids for various Reynolds numbers, $\text{Re} = UL_c/\vartheta$, where L_c is the height of the cavity. First, a nonuniform grid of bilinear elements (30×30 for $\text{Re} = 100$ or 1000 and 50×50 for $\text{Re} = 5000$) is taken, where both velocity and pressure are approximated by bilinear Lagrange polynomials. Next, we analyze a nonuniform grid of biquadratic elements (15×15 for $\text{Re} = 100$ or 1000 and 25×25 for $\text{Re} = 5000$), where the velocity field is interpolated by biquadratic Lagrange polynomials, whereas the pressure field, only by bilinear ones. The results obtained are given in Figure 1 in terms of streamlines and pressure contours (a reference point at the middle of the bottom wall) at chosen early times of the process and at the final steady state. The dimensionless time used in Figure 1 is calculated as $\tau = Ut/L_c = (\vartheta\text{Re})t/L_c^2$. Both discretization cases are almost graphically undistinguished. Transient and steady state solutions are in good agreement with the results reported by others [5, 6, 14]. Indeed, the velocity and pressure predictions for $\text{Re} = 100$ at dimensionless time $\tau = 5.0$ are very close to those obtained through the use of an equal-order FEM interpolation on a triangular grid along with explicit Euler calculations of an intermediate velocity and implicit scheme for final velocity and pressure fields [5]. Steady state velocity profiles along vertical and horizontal centerlines and extrema of the stream function of the primary vortex are also in good agreement with those given in Refs. [6, 14] (see Figure 2 and Table 1). Moreover, Figure 1 shows that no spurious pressure mode is observed. Therefore one can conclude that the severe restrictions of Babuska Brezzi stability criteria [13] can be sidestepped in this algorithm, where the pressure gradient is completely discarded in the computation of the intermediate velocity field.

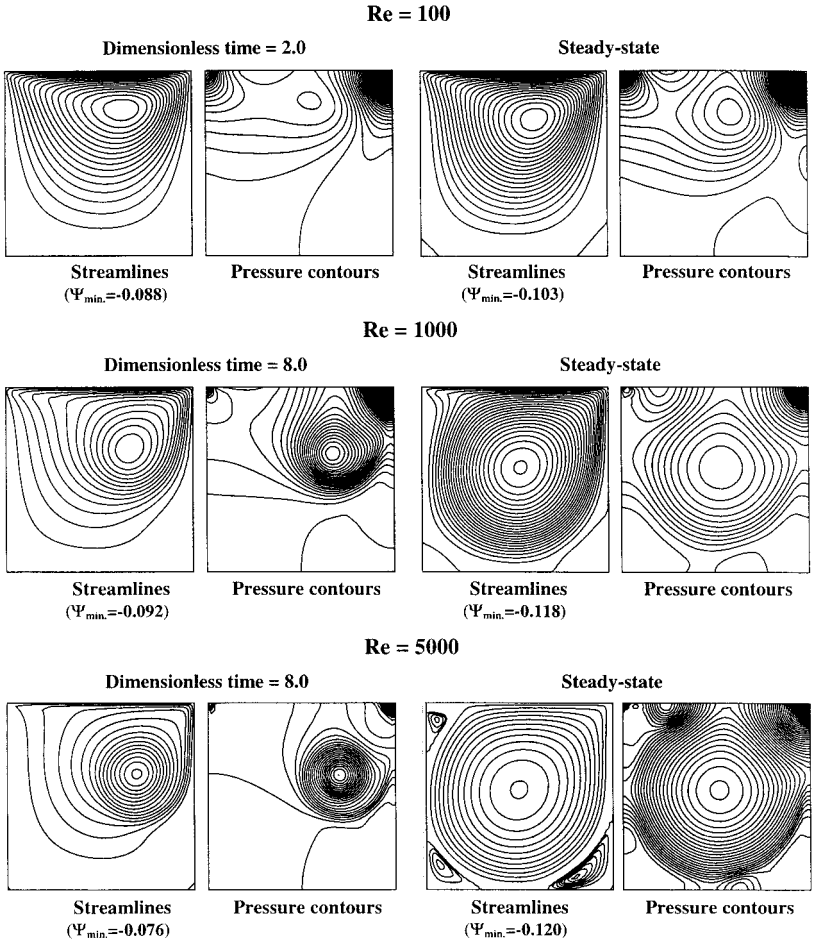

Figure 1. Lid-driven cavity problem: streamlines and pressure contours for various Re at early times of the process and at steady state.

To verify the algorithm in the case of a coupled fluid flow and heat transfer problem, the laminar natural convection in a square enclosure is solved for various Rayleigh numbers (Ra) with Prandtl number Pr = 1.0 and with the assumption that the Boussinesq approximation [12] is valid. The lower and upper walls are considered adiabatic, whereas the vertical walls are kept at uniform but different temperatures. The left hot wall is at $\tilde{T}_h = 0.5$, and the right cold one is at $\tilde{T}_c = -0.5$, where $\tilde{T}$ is dimensionless temperature defined as $\tilde{T} = (T - \Delta T_{av})/(T_h - T_c)$ with $\Delta T_{av} = (T_h + T_c)/2$. The domain is covered with an irregular grid (denser near the walls) of 40×40 bilinear elements. The obtained steady state flow pattern, pressure, and dimensionless temperature fields are presented in Figure 3. They are in good agreement with calculations published elsewhere (e.g., [6]).

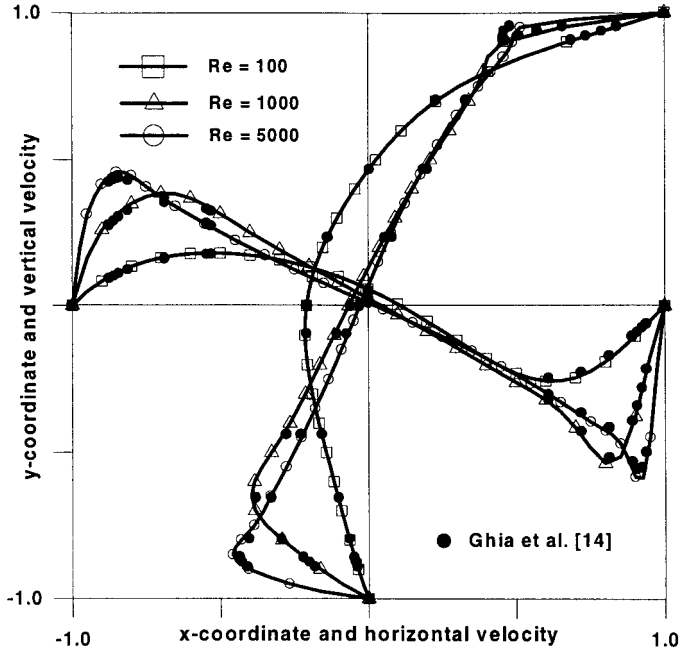

Figure 2. Profiles of dimensionless horizontal and vertical velocities along centerlines of the cavity.

CODE VALIDATION ANALYSIS

To find out how closely the real problem is represented by the physical model (incompressibility assumption, the method of modeling phase change and buoyancy effects) and by its computer simulation, natural convection in freezing water in a differentially heated cube-shaped enclosure is studied experimentally. The empirical results are then compared with calculations.

Two opposite vertical walls, made of black anodized metal, are kept at uniform but different temperatures. The hot wall is at 10°C, whereas the cold one is at 0°C in the case of natural convection and at −10°C when water solidification driven by convection and conduction is studied. The remaining four walls, made of 6 mm Plexiglas, are considered as thermal insulators of low conductivity and thermal diffusivity comparable to that of water.

Table 1. Extrema of the primary vortex stream function

	$Re = 10^2$	$Re = 10^3$	$Re = 5 \times 10^3$
Present method	−0.103	−0.119	−0.119
Ramaswamy et al. [5, 6]	−0.103	−0.118	−0.117
Ghia et al. [14]	−0.013	−0.118	−0.119

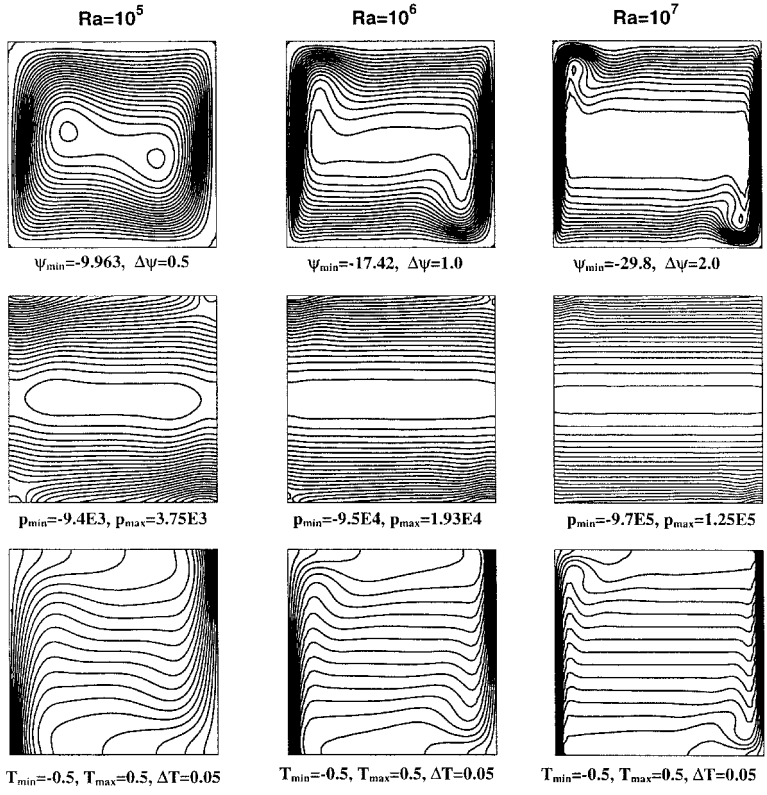

Figure 3. Streamlines, pressure contours, and isotherms for steady state natural convection in a square cavity.

Water is a fluid that does not obey the Boussinesq approximation, for its density near 4°C is a nonlinear function of temperature (Figure 4*a*). Moreover, the water density anomaly, with its maximum at 4°C, creates a complex flow pattern that contains two different circulation regions, one of clockwise and the second of counterclockwise circulation (Figure 4*b*). Fortunately, the assumption of incompressibility can be accepted here, as the density change of water is negligible ($< 0.03\%$) in the analyzed temperature range (0°–10°C). This means that the presented FEM algorithm, valid only for an incompressible fluid, can be applied.

Two different cases of thermal boundary conditions are investigated (Figure 4*c*). In the first, the domain of interest is restricted to the interior of the cavity, where natural convection and freezing of water are analyzed under the assumption that the horizontal walls are adiabatic. In the second case, a conjugate heat transfer model is considered: natural convection and phase change of water are calculated simultaneously with heat conduction in the Plexiglas walls and the convective boundary conditions shown in Figure 4*c*.

The complex local flow structure necessitates application of sophisticated full-field acquisition experimental techniques to get local transient velocity and temperature fields, exact and reliable enough to be a reference standard in

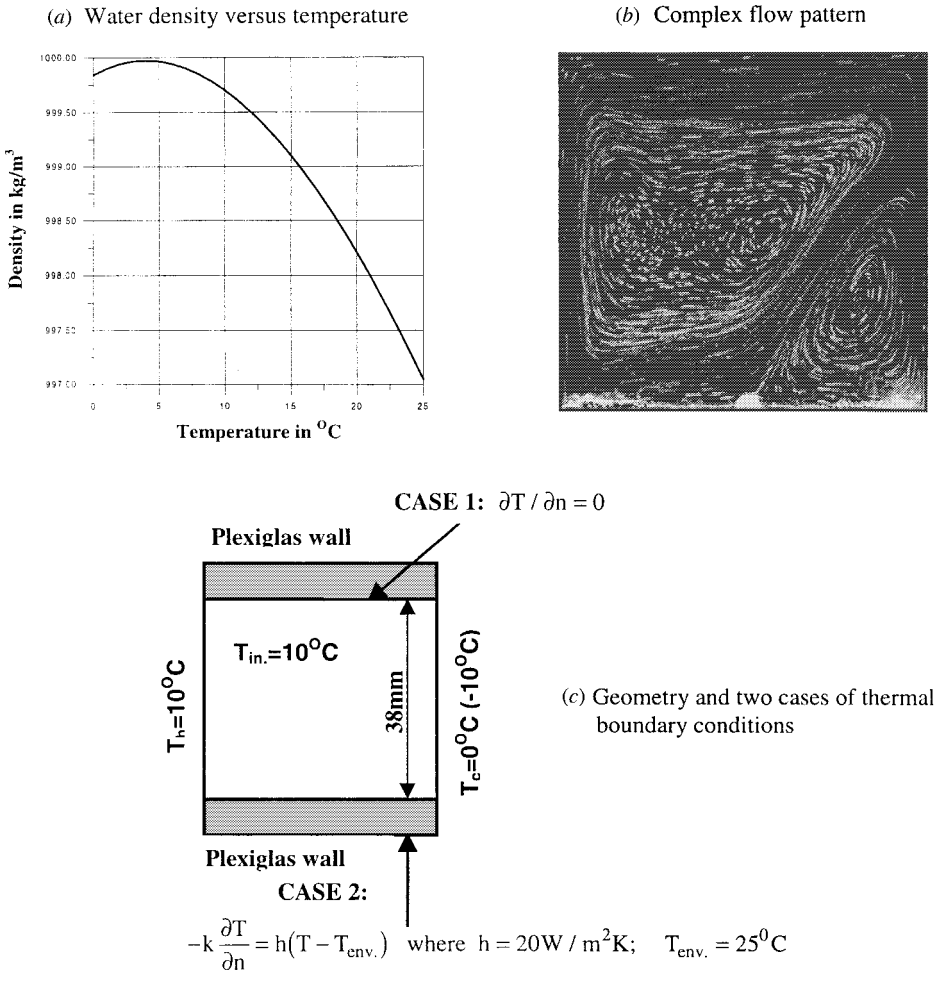

Figure 4. Problem specification for natural convection of freezing water.

comparison with numerical results. The method applied in the experimental study is based on the use of a thermochromic liquid crystal (TLC) suspended in water as seeding. Digital particle image velocimetry (PIV) combined with digital color analysis allows simultaneous measurement of two-dimensional velocity and temperature fields [15, 16].

A sketch of the experimental apparatus is shown in Figure 5. The flow field in the analyzed cavity filled with distilled water is illuminated by a 2 mm thick sheet of white light from a specially constructed halogen lamp, and observed in the perpendicular direction. The 24-bit color images (of 768 × 564 pixels) from a digital color camera are acquired using a Pentium computer. A system of three stepping motors, controlled by the computer, allows the acquisition of images at several horizontal and vertical cross sections. Thus a three-dimensional analysis of

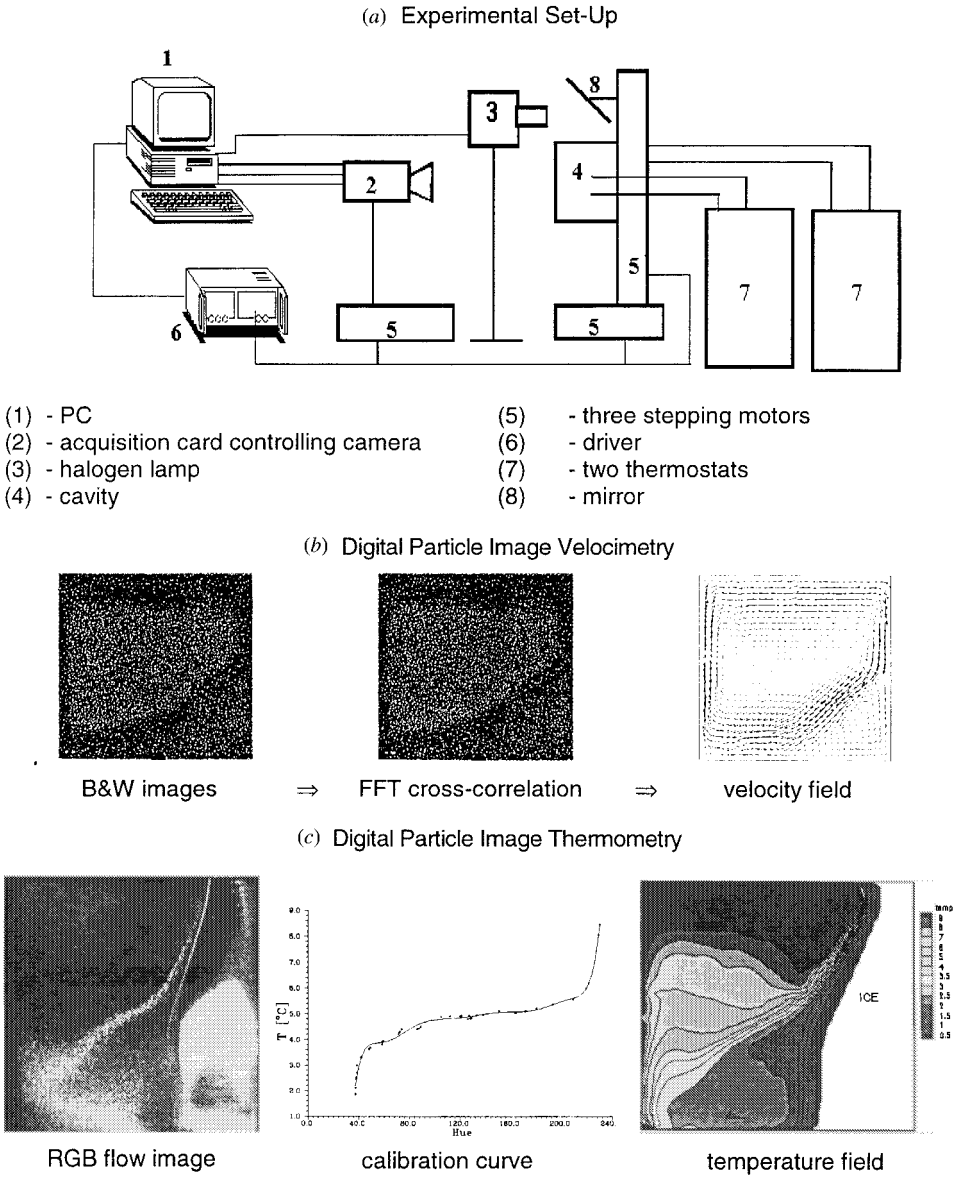

Figure 5. Test apparatus and experimental procedure.

the whole flow domain can be carried out. Thermostats control the temperature of the isothermal walls.

To obtain the velocity field, color images of liquid-crystal tracers are transformed into black-and-white intensity images. A pair of such images taken at the given time interval is cross correlated (using fast Fourier transform (FFT)) to get local displacements. After dividing them by the time interval, the local velocity is

obtained in the two-dimensional plane (Figure 5). Temperature visualization is based on the property of some liquid-crystal materials to reflect definite colors at specific temperatures and viewing angle. The color change for the TLC ranges from clear at ambient temperature, through red as temperature increases, and then to yellow, green, blue, and finally, clear again at the highest temperature. Temperature measurement is based on a digital color analysis of RGB red-green-blue images of the TLCs seeded flow field. Incoming RGB signals are transformed pixel by pixel into hue, saturation, and intensity. Temperature is then determined by relating the hue to temperature through the calibration curve (Figure 5). More details about experimental arrangements and procedure can be found in Refs. [15, 16].

Natural Convection of Pure Water

First, we consider the problem of natural convection (without phase change) in the cavity filled with pure water at an initial temperature of 10°C. A sudden drop of temperature of one of the lateral wall to 0°C causes buoyancy forces to arise. The horizontal walls are considered adiabatic (Figure 4, case 1). The results obtained on a regular 40 × 40 bilinear equal-order finite element grid are given in Figure 6, in terms of temporal flow pattern and temperature field at various times of the process. Regular thermal convection, characterized by a large clockwise circulation, is initiated when cooling of the cold wall starts. After a short time (about 100 s), the second, counterclockwise circulation becomes visible in the lower, cold corner. Because of the density anomaly, the cold fluid in this corner moves up along the cold wall. Its interaction with the hot liquid in an upper part of

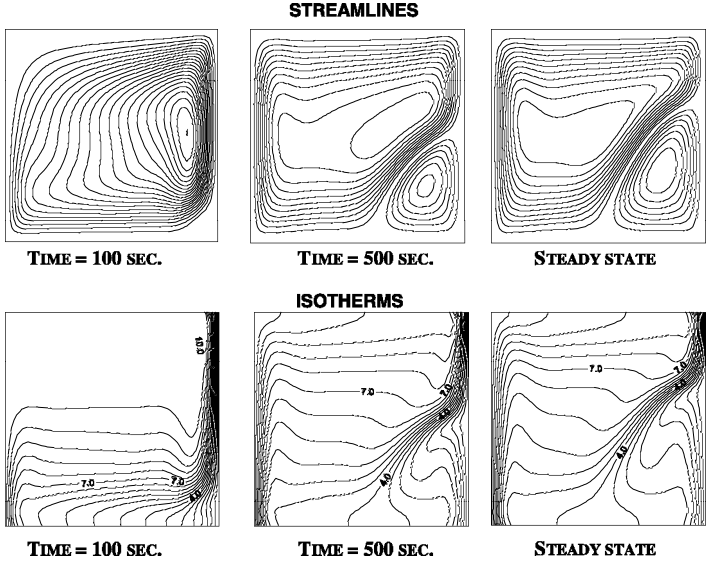

Figure 6. Natural convection of pure water in enclosure with adiabatic horizontal walls.

the cavity reverses buoyancy forces and redirects the flow back to the bottom and to the cold wall. This circulation, initially limited to the small region, grows in time, penetrating deeper and deeper and into the cavity center. Within a few minutes, it pushes the main, clockwise convection back to the hot wall region. After about 20 min of competing effects of positive and negative buoyancy forces, a steady state is obtained. This is characterized by a relatively large regular flow circulation, transporting hot liquid from the left wall up to the top, and the second smaller counterclockwise circulation, filling approximately one-fifth of the cavity (Figure 6).

The assumption made in the calculations that lower and upper Plexiglas walls are adiabatic is not very precise. In the experimental arrangement, these walls are not perfectly thermally insulated. Also heat fluxes along relatively thick walls cannot be completely neglected. To include more realistic boundary conditions into the presented computer simulation code, the numerical model has been further developed to simultaneously calculate both natural convection in water and conduction in the Plexiglas walls. The results of this conjugate heat transfer analysis are depicted in Figure 7. Comparison of the thus obtained flow pattern to that given in Figure 6 shows the significant influence of thermal boundary conditions on the velocity and temperature fields in the cavity. It is seen that from the beginning of the process the counterclockwise vortex in Figure 7 is smaller than the one presented in Figure 6. Its shape is also closer to the one observed in the experiment (Figure 8).

This observation is confirmed in detail by studying the local vertical velocity distribution along the dimensionless X coordinate, where $X = x/L_c$ and L_c is the cavity width equal to 0.038 m. The steady state distribution of this velocity is shown

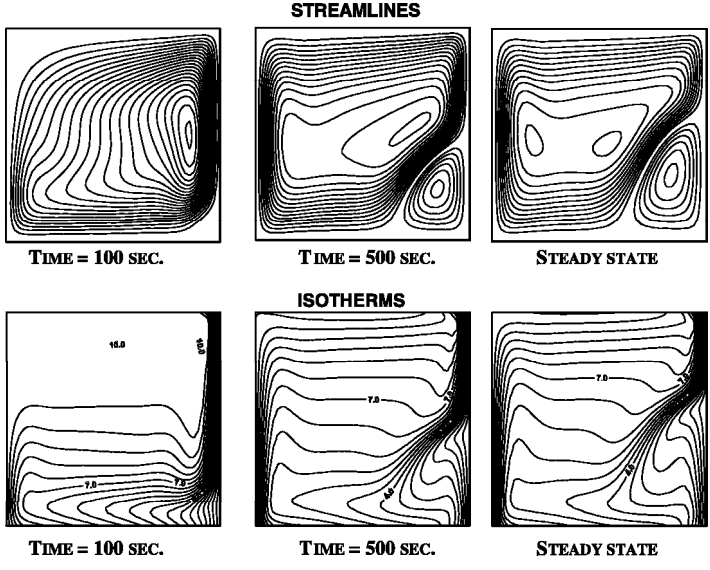

Figure 7. Natural convection of pure water in enclosure with conduction through horizontal walls.

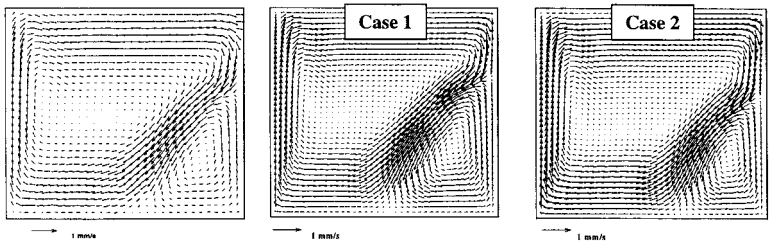

Figure 8. Experimental and calculated velocity fields for steady state natural convection of water.

in Figure 9 in three selected horizontal cross sections of the enclosure for both cases of thermal boundary conditions. The velocity obtained upon the assumption that the horizontal walls of the cavity are adiabatic is visibly different from the experimental findings, particularly in the central cross section of the analyzed domain. On the other hand, very good agreement between measurements and calculations is obtained in the case of the conjugate heat transfer analysis (case 2). This lends strong support to the modeling of the process as a conjugate circumstance.

Natural Convection in Freezing Water

Next, the more challenging problem of natural convection in freezing water is analyzed. Velocity and temperature fields of the above-discussed final steady state convection in pure water are used as initial conditions. Numerical results are given in Figures 10 and 11. Sudden change of temperature of the lateral cold wall from $0^{\circ}C$ to $-10^{\circ}C$ causes ice creation near this wall and shifts two competing vortices toward the hot lateral wall. The cold counterclockwise circulation at the lower corner is crucial for the shape of the growing ice front, insulating its surface from the hot fluid. Therefore the initially almost plane surface of the ice deforms in time, growing faster in its lower part. As the ice layer expands, the flow domain changes in time. Hence both competing vortices vary in shape, and their centers move toward the hot lateral wall.

Streamlines, temperature field, and water/ice temporal front position (a curve where the total enthalpy is equal to half of the fusion one, and $f = 0.5$) at various times of the solidification process are given in Figure 10 for the case of adiabatic horizontal walls (case 1 in Figure 4). The corresponding results of the conjugate heat transfer model (case 2 in Figure 4), where convection with a liquid-solid phase change in the cavity and conduction in the Plexiglas walls are calculated simultaneously, are depicted in Figure 11. In the latter case the counterclockwise vortex is smaller, and the shape of the ice is different. This means that in the case of water solidification the impact of even minor changes of thermal boundary conditions is more significant than in the previously analyzed convection without phase change.

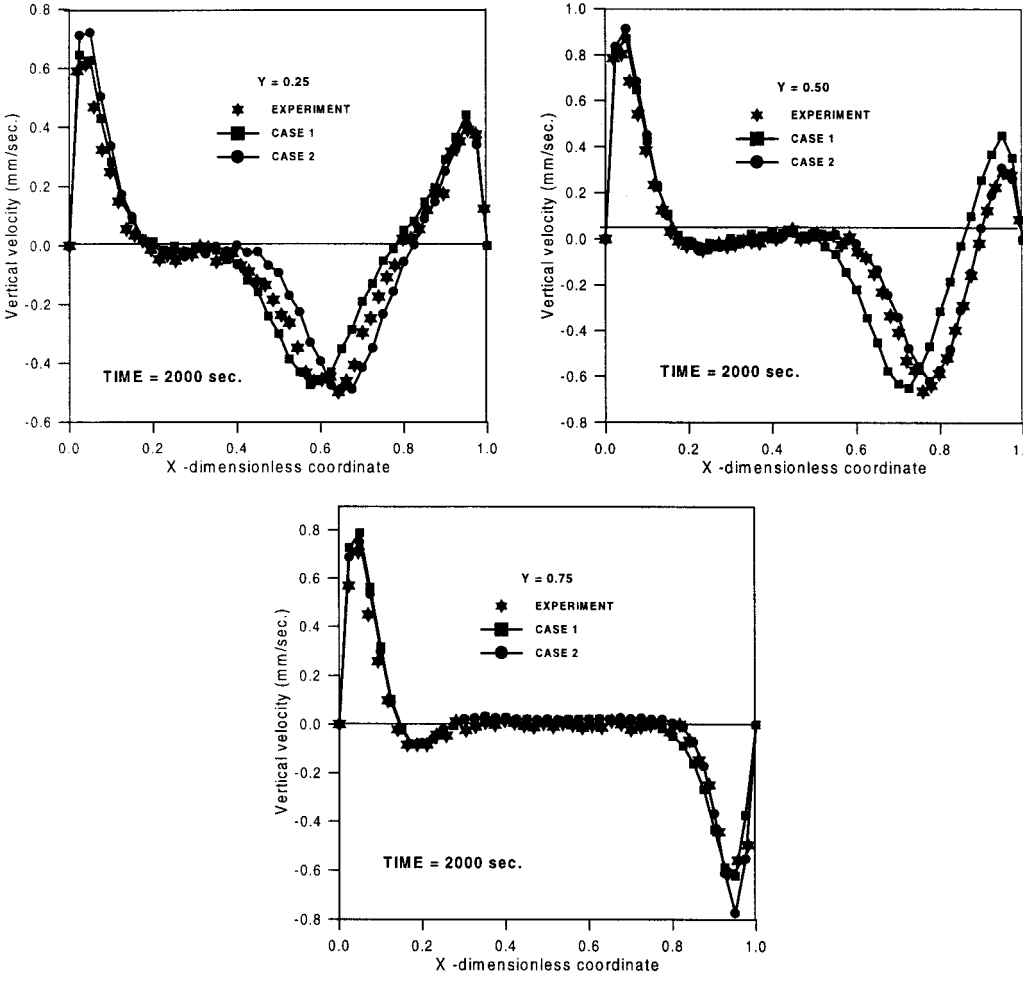

Figure 9. Comparison of experimental and numerical results for steady state local vertical velocity.

The conjugate heat transfer model gives results that are closer to those registered by PIV and digital particle image thermometry (DPIT) techniques. This is further confirmed in Figures 12 and 13. The local vertical velocity and the ice shape, calculated for both cases of the thermal boundary conditions, are compared there with the pertinent experimental findings at an early time of the process (after 500 s) and at steady state (after 3000 s).

The conjugate heat transfer calculations give the flow structure that is optically very similar to the one from the experiment (Figure 14). However, more detailed comparative analysis, given in Figures 12 and 13, reveals that some incongruity in the temporal ice shapes and local velocities still occurs, particularly in a central part of the cavity.

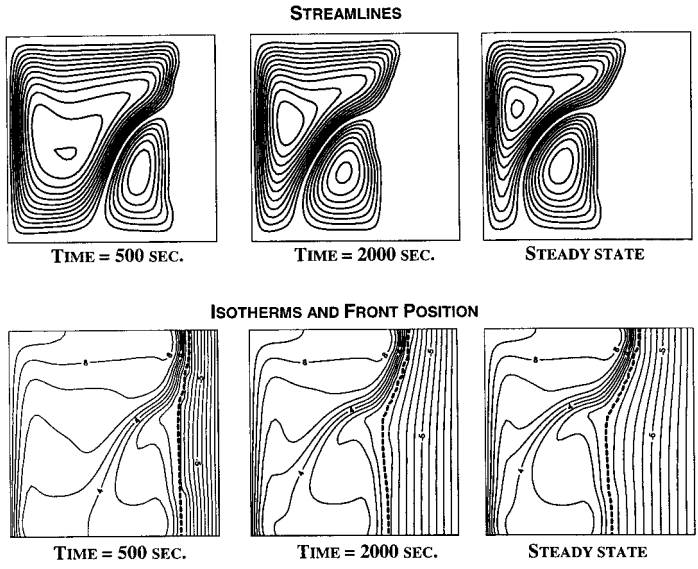

Figure 10. Water solidification controlled by convection and conduction for case 1: adiabatic horizontal walls.

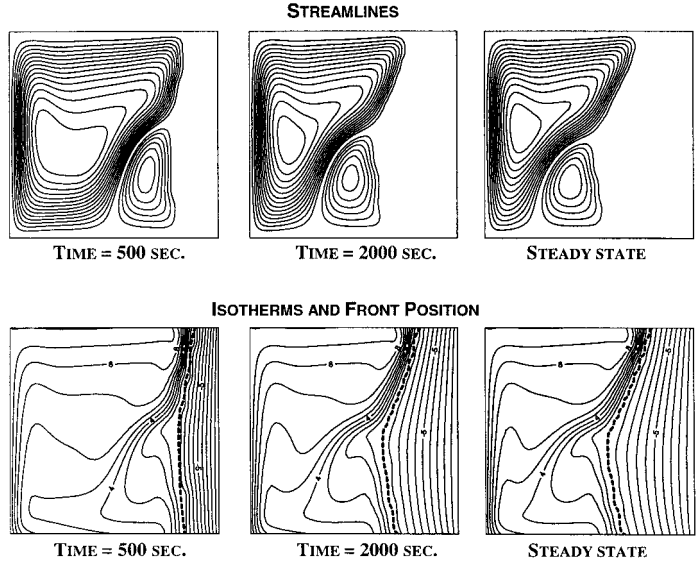

Figure 11. Water solidification controlled by convection and conduction for case 2: conjugate heat transfer model.

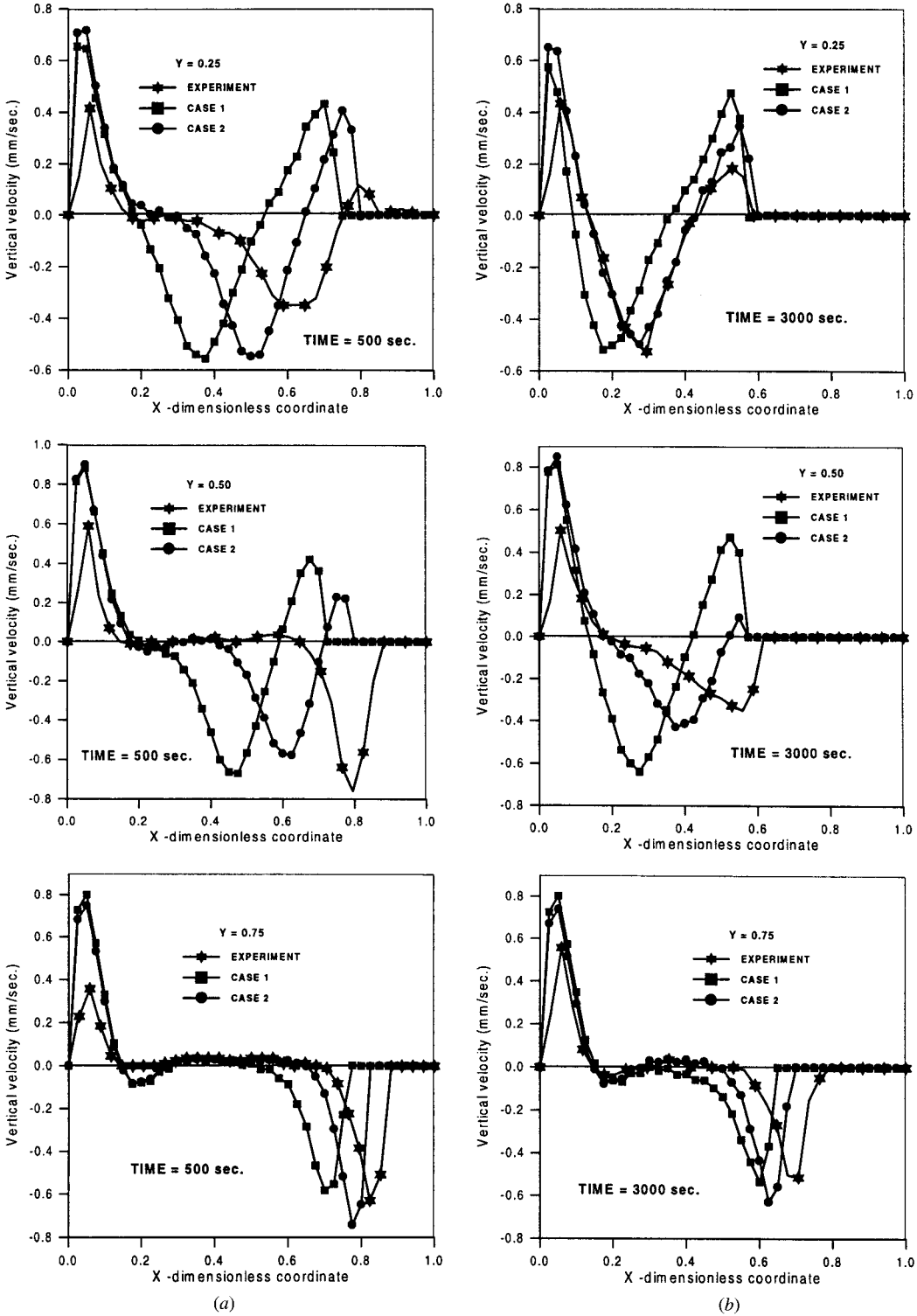

Figure 12. Local vertical velocity comparisons: calculations versus experimental results.

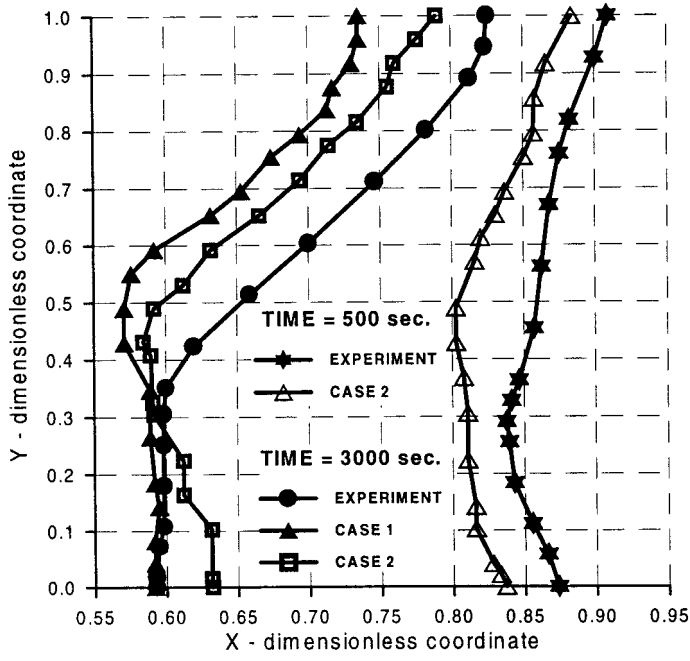

Figure 13. Ice/water temporal front position: calculations versus experimental results.

DISCUSSION AND CONCLUDING REMARKS

One of the possible reasons for this visible but not significant disparity between measurements and calculations might be the effect of water supercooling. This is an observed effect in the experiment but is not included in the numerical model. To elucidate the problem, experimental results are shown in Figure 15 at the onset of water freezing. A sudden drop of the lateral wall temperature (to $T_c = -10^{\circ}C$) immediately generates a counterclockwise vortex with upward convection of the supercooled fluid. After the first 40–60 s, the supercooled water plume may even cover half the upper surface. The temperature of water drops below $-7^{\circ}C$, but, after about 240 s, sudden freezing of the supercooled water occurs. Then, within the next 10–15 s, the clockwise convection melts the excessive ice at the lid and recovers the regular plane propagation of the ice front. This effect retards the solidification process, significantly changing the flow pattern in the cavity at early times in the process. This effect can alter the front propagation at longer times. Therefore some numerical modeling of a nucleation delay time seems necessary.

Moreover, when water freezes in a small cavity, high sensitivity of flow structure and thus of the temperature field, to thermophysical properties and boundary conditions is observed. This means that calculations can be significantly dependent on such effects as: (1) inaccuracy of available thermophysical data and convective heat transfer coefficient, (2) nonhomogeneity and layering of a solid

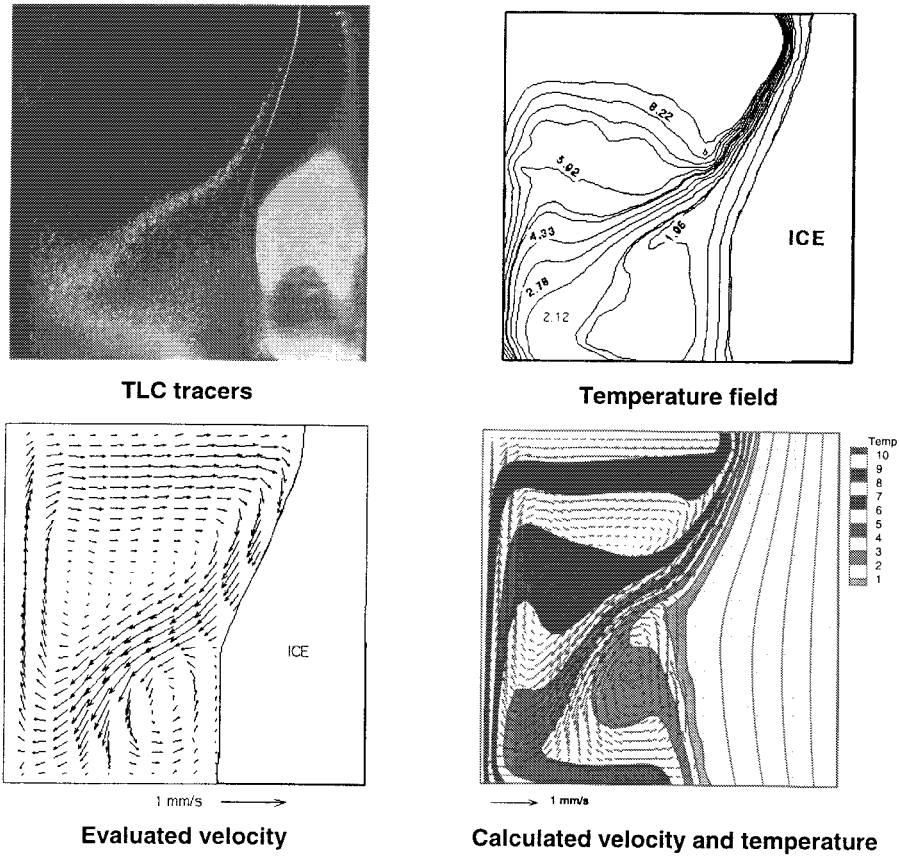

Figure 14. Experimental results versus conjugate heat transfer calculations for water solidification driven by convection and conduction.

structure, (3) nonideal thermal contact between ice and cold walls, (4) thermal boundary layer at the phase interface, and (5) nonuniform temperature of "isothermal" walls.

Some differences between numerical results and experimental data can be also explained by the limitation of computational analysis to two-dimensional geometry (in the experiment, some side wall effects are observed) as well as by some freedom of definition of mushy region properties in the enthalpy-porosity approach. However, the results of calculations given in Figure 16, in terms of the streamlines and details of the local vertical velocity and of the water/ice interface position, show that the value of the porosity constant C is of rather minor significance in the case of isothermally solidifying water.

Therefore one can conclude that when a detailed code validation analysis is carried out, by comparing calculated temporal and local variables with their experimental counterparts, a crucial problem emerges: the authenticity of material

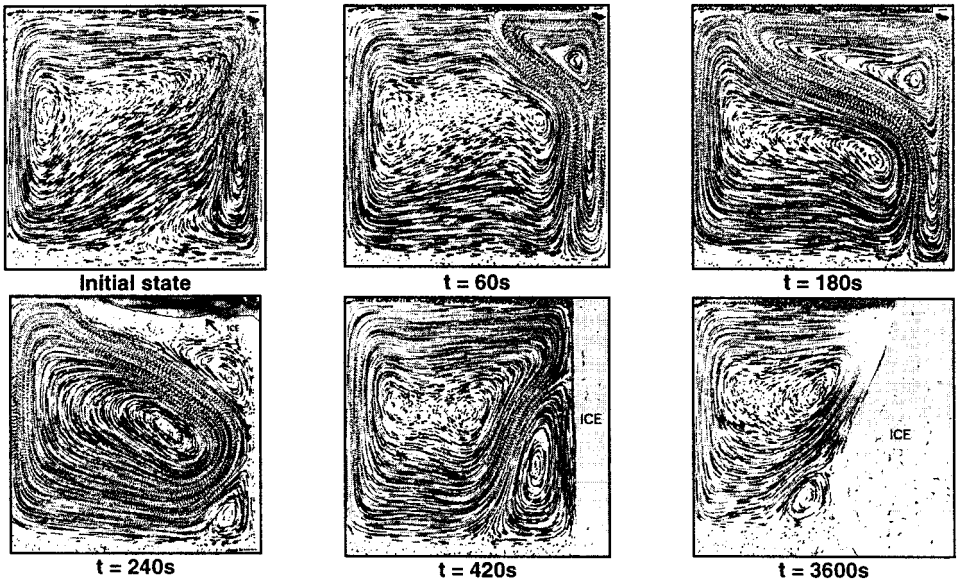

Figure 15. Observed effect of water supercooling by the PIV technique.

data and of boundary and initial conditions, i.e., consistency between the real and the idealized.

The conventional FEM formulation for the incompressible Navier-Stokes equations, termed by Gresho [4] the "honest GFEM," is based on implicit schemes applied to fully coupled continuity and momentum equations discretized in space via mixed FEM interpolations [1, 2]. This approach, where the whole set of fluid mechanics equations must be treated simultaneously, requires the solution of a very large nonsymmetric matrix system by direct solvers. Thus it demands a substantial amount of computer storage and CPU time, even when specialized sparse matrix solvers are employed. Therefore explicit and semi-explicit time split algorithms have been borrowed from the finite difference approach, and they have been further developed in the FEM context to retain all flexibility of the FEM discretization [4–6]. It is proved that the explicit treatment of the advection and the sequential solving algorithm, where a single large coupled system of equations for velocity components and pressure is replaced by several smaller, symmetric linear systems solved sequentially, provides considerable savings of computer storage and computation times (e.g., [4–6]). The focus of this paper is on the extension of the semi-implicit projection method [4] through the combination of this solving technique with the enthalpy-porosity model on a fixed grid. Thus a computationally efficient and robust tool is obtained for FEM analysis of solid-liquid phase change phenomena driven by convection and conduction. The accuracy of the model developed has been verified by solving two commonly used benchmark problems, mainly in order to check whether low equal-order FEM grids used along with the projection method do not produce spurious pressure modes. The results obtained for the lid-driven cavity flow and for the Boussinesq natural convection in a square

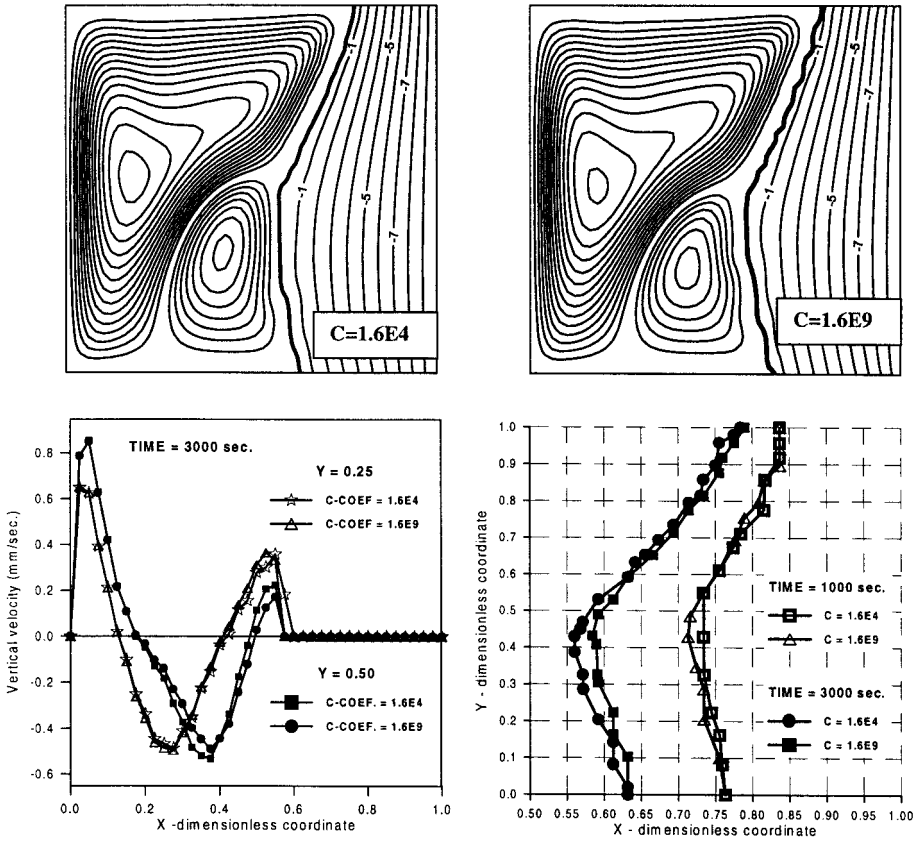

Figure 16. Influence of porosity constant C on calculated flow structure, local vertical velocity, and shape of the interface.

enclosure show that the severe restrictions of the Babuska-Brezzi stability condition can be sidestepped in the presented algorithm. Therefore this computational technique has been further used to solve the more challenging problem of natural convection of freezing water. To provide a detailed analysis of the model validation, we have performed our own experimental study to create a new reference standard. Based on up-to-date sophisticated full-field acquisition techniques, we have acquired data for temporal and local velocity and temperature fields both for natural convection of pure water in the temperature range including the density anomaly point and for pure water freezing in a cavity. Comparisons between thus obtained experimental findings and the calculations reveal that a computationally efficient low-order FEM model based on a combination of the projection method and the enthalpy-porosity approach provides results that are in very good agreement with the measurements in the case of pure natural convection of water. Moreover, in the case of water solidification, the calculated local velocity and temperature fields are close to those from the PIV and DPIV techniques, indicting the validity and accuracy of the presented model and its numerical scheme. Further

improvement of the congruity of measured and calculated results is possible through more precise modeling of real initial and boundary conditions.

REFERENCES

1. C. Taylor and T. J. R. Hughes, *Finite Element Programming of the Navier-Stokes Equations*, Pineridge Press, Swansea, 1981.
2. A. S. Usmani, R. W. Lewis, and K. N. Seetharamu, Finite Element Modelling of Natural Convection–Controlled Change Phase, *Int. J. Numer. Methods Fluids*, vol. 14, pp. 1019–1036, 1992.
3. A. J. Chorin, Numerical Solution of Navier-Stokes Equations, *Math. Comput.*, vol. 22, pp. 745–762, 1968.
4. P. M. Gresho, On the Theory of Semi-Implicit Projection Methods for Viscous Incompressible Flow and Its Implementation via a Finite Element Method That Also Introduces a Nearly Consistent Mass matrix, Part 1: Theory, *Numer. Heat Transfer, Part A*, vol. 29, pp. 49–63, 1996.
5. B. Ramaswamy and M. Kawahara, An Efficient Element Finite Scheme for Incompressible Viscous Fluid Flow, *Indian J. Technol.*, vol. 126, pp. 1–13, 1988.
6. B. Ramaswamy, T. C. Jue, and J. E. Akin, Semi-Implicit and Explicit Finite Element Schemes for Coupled Fluid/Thermal Problems, *Int. J. Numer. Methods Eng.*, vol. 34, pp. 675–692, 1992.
7. O. Axelsson and V. A. Barker, *Finite Element Solution of Boundary Value Problems*, Academic Press, Orlando, Florida, 1984.
8. V. R. Voller, M. Cross, and N. C. Markatos, An Enthalpy Method for Convection/Diffusion Phase Change, *Int. J. Numer. Methods Eng.*, vol. 24, pp. 271–284, 1987.
9. V. R. Voller and C. Prakash, A Fixed Grid Numerical Modeling Methodology for Convection-Diffusion Mushy Region Phase-Change Problems, *Int. J. Heat Mass Transfer*, vol. 30, pp. 1709–1719, 1987.
10. A. D. Brent and V. R. Voller, Enthalpy-Porosity Technique for Modeling Convection-Diffusion Phase Change: Application to the Melting of a Pure Metal, *Numer. Heat Transfer*, vol. 13, pp. 297–318, 1988.
11. C. R. Swaminathan and V. R. Voller, General Enthalpy Method for Modeling Solidification Processes, *Metall. Trans. B*, vol. 23B, pp. 651–664, 1992.
12. B. Gebhart, Y. Jaluria, R. L. Mahajan, and B. Sammakia, *Buoyancy Induced Flows and Transport*, Hemisphere, New York, 1988.
13. O. C. Zienkiewicz and R. L. Taylor, *Finite Element Method*, 4th ed., McGraw-Hill, London, 1989.
14. U. Ghia, K. Ghia, and C. Shin, High-Re Solutions for Incompressible Flow Using the Navier-Stokes Equations and a Multi-Grid Method, *J. Comput. Phys.*, vol. 48, pp. 387–401, 1982.
15. T. A. Kowalewski, A. Cybulski, and M. Rebow, Particle Image Velocimetry and Thermometry in Freezing Water, presented at the 8th International Symposium on Flow Visualization, Sorrento, 1998.
16. T. A. Kowalewski, Experimental Validation of Numerical Codes in Thermally Driven Flows, in G. Vahl Davis and E. Leonardi, eds., *CHT-97: Advances in Computational Heat Transfer*, pp. 1–16, Begell House, New York, 1998.